21. G. S. Moeck *et al.*, *Mol. Microbiol.* **22**, 459 (1996).
22. G. S. Moeck, J. W. Coulton, K. Postle, *J. Biol. Chem.* **272**, 28391 (1997).
23. P. E. Klebba *et al.*, *J. Bioenerg. Biomembr.* **25**, 603 (1993); R. J. Kadner and K. J. Heller, *J. Bacteriol.* **177**, 4829 (1995).
24. G. S. Moeck and J. W. Coulton, *Mol. Microbiol.* **28**, 675 (1998).
25. Strictly conserved side-chain residues that are thought to be involved in the surface diffusion of ferrichrome-iron through the putative channel-forming region may be Arg^{297} and Asn^{299} from β7; Asp^{358}, Gln^{360}, and Asp^{379} from β9; and Asn^{436}, Gln^{438}, and Gln^{440} from β10.
26. G. Adam and M. Delbrück, in *Structural Chemistry and Molecular Biology*, A. Rich and N. Davidson, Eds. (Freeman, San Francisco, 1968), pp. 198–215.
27. H. Killmann, R. Benz, V. Braun, *J. Bacteriol.* **178**, 6913 (1996).
28. Strand β7 is composed of residues 294 to 317, L4 is composed of residues 318 to 339, and strand β8 is composed of residues 340 to 366.
29. T. Schirmer *et al.*, *Science* **267**, 512 (1995); D. Forst *et al.*, *Nature Struct. Biol.* **5**, 37 (1998).
30. A. Mademidis *et al.*, *Mol. Microbiol.* **26**, 1109 (1997).
31. A more complicated mechanism could avoid the possible loss of the ferrichrome-iron into the external medium after the formation of the FhuA-TonB complex by the steric blockage of the surface-located pocket. However, the TonB-dependent binding and uptake of the FhuA-specific toxin colicin M through FhuA would require that the putative channel-forming region remain open from the external environment to the periplasm for an extended period of time and therefore would contradict such a mechanism [C. J. Lazdunski *et al.*, *J. Bacteriol.* **180**, 4993 (1998); R. M. Stroud *et al.*, *Curr. Opin. Struct. Biol.* **8**, 525 (1998)].
32. M. L. Guerinot, *Annu. Rev. Microbiol.* **48**, 743 (1994).
33. A. Ghosh *et al.*, *Chem. Biol.* **3**, 1011 (1996).
34. Single-letter abbreviations for the amino acid residues are as follows: A, Ala; C, Cys; D, Asp; E, Glu; F, Phe; G, Gly; H, His; I, Ile; K, Lys; L, Leu; M, Met; N, Asn; P, Pro; Q, Gln; R, Arg; S, Ser; T, Thr; V, Val; W, Trp; and Y, Tyr.
35. Because FhuA is difficult to purify to homogeneity in large amounts, one prerequisite for crystallization and subsequent structural analysis by x-ray crystallography was the development of an overexpression system and efficient protocols for the rapid purification of FhuA [A. D. Ferguson *et al.*, *Protein Sci.* **7**, 1636 (1998)]. A recombinant FhuA was constructed by splicing a hexahistidine tag and three additional residues (SHHHHHHGS) (*34*) at a previously identified surface location (amino acid 405) [G. S. Moeck *et al.*, *J. Bacteriol.* **176**, 4250 (1994)]. Functional assays confirmed (*21*) that the protein $FhuA405.H_6$ (native FhuA) is fully active as a bacteriophage receptor and is also active for TonB-dependent ferrichrome-iron transport at levels comparable to those of the wild type. To generate selenomethionyl-labeled FhuA (SeMet-FhuA), plasmid pHX405 was transformed into the *met*⁻ auxotrophic *E. coli* strain DL41 and grown as recommended [S. Doublié, *Methods Enzymol.* **276**, 523 (1997)].
36. S. J. Angyal, L. Odier, M. E. Tate, *Carbohydr. Res.* **266**, 143 (1993).
37. Phase information was derived from multiple anomalous dispersion (MAD) [W. A. Hendrickson, *Science* **254**, 51 (1991)] data that were measured at three wavelengths that corresponded to the point of inflection, the peak of the selenium absorption profile, and a remote point. All data were reduced and processed with the XDS software package [W. Kabsch, *J. Appl. Crystallogr.* **21**, 916 (1988)]. The 10 selenium sites were located with SOLVE [T. C. Terwilliger and J. Berendzen, *Acta Crystallogr.* **D53**, 571 (1997)], and MAD phases were obtained with SOLVE and SHARP [E. de La Fortelle and G. Bricogone, *Methods Enzymol.* **276**, 472 (1997)]. Initial phases, which were calculated to a resolution of 3.05 Å, were improved by solvent flattening with the program DM [K. Cowtan, *Acta Crystallogr.* **D50**, 760 (1994)]. The resulting electron density maps were of sufficient quality to build a model with the program O [T. A. Jones *et al.*, *Acta Crystallogr.* **A47**, 110 (1991)] and unambiguously place a ferrichrome-iron molecule and a LPS molecule. The model was refined with the programs X-PLOR [A. T. Brünger, X-PLOR 3.1 (Yale University, New Haven, CT, 1992)] and CNS [A. T. Brünger *et al.*, *Acta Crystallogr.* **D54**, 905 (1998)] and was used to solve the structure of FhuA to a resolution of 2.5 Å by difference Fourier techniques. Standard protocols for simulated annealing and minimization as implemented in CNS were used for refinement. Individual restrained B-factor refinement was justified as judged by a substantial drop in R_{free} [A. T. Brünger, *Nature* **355**, 472 (1992)]. The current FhuA model contains residues 19 to 723, 1 LPS, and 99 water molecules. The average B factors for main-chain and side-chain atoms and the LPS molecule are 65, 67, and 78 $Å^2$, respectively. The FhuA model was used in the refinement of the FhuA–ferrichrome-iron complex to a resolution of 2.7 Å. The current model for the FhuA–ferrichrome-iron complex contains residues 19 to 723, 1 LPS, 1 ferrichrome-iron molecule, and 52 water molecules. The average B factors for main-chain and side-chain atoms, the LPS, and ferrichrome-iron molecules are 63, 66, 75, and 49 $Å^2$, respectively. Refinement is not complete for both structures. For the FhuA model, the R_{cryst} is 24.2% (48,359 reflections), and the R_{free} is 28.3% (2309 reflections); for the FhuA–ferrichrome-iron complex, the R_{cryst} is 23.2% (37,362 reflections), and the R_{free} is 28.1% (1532 reflections). All residues lie in allowed regions of the Ramachrandran plot, and all residues that are explicitly mentioned in the text reside in good electron density. Protein Data Bank accession codes are 2fcp and 1fcp for FhuA and the FhuA–ferrichrome-iron complex, respectively.
38. All figures were prepared with the programs MOLSCRIPT [P. Kraulis, *J. Appl. Crystallogr.* **24**, 946 (1991)] and Raster-3D [E. A. Merrit and D. J. Bacon, *Methods Enzymol.* **277**, 505 (1997)], except for Fig. 3, which was prepared with the program O.

39. We gratefully acknowledge A. Svensson at MAX-lab II and A. Thompson at the European Radiation Synchrotron Facility for their assistance and generous support during data collection; E. A. Meighen for providing *E. coli* strain DL41; P. A. Karplus for a critical reading of the manuscript; J. Wang for genetic constructs; V. Braun and H. Killmann for bacterial strains and discussions; A. Patel for his assistance with protein purification; J. Breed for crystallization trials and a critical reading of the manuscript; D. M. Allan and J. A. Kashul for editing, K. Hegetschweiler for providing *cis*-inositol; and B. Herrmann, A. Hirsch, C. Peinelt, O. Seth, and J. Telioriclis, who made important contributions to the early phase of this project. This work was supported by the Deutsche Forschungsgemeinschaft (W.W.); by the Medical Research Council, Canada (grant MT-14133 to J.W.C.); and by NATO International Collaborative Research grant 960082. A.D.F. is the recipient of a Deutscher Akademischer Austauschdienst Grant for Study and Research.

23 October 1998; accepted 13 November 1998

Structure of the MscL Homolog from *Mycobacterium tuberculosis*: A Gated Mechanosensitive Ion Channel

Geoffrey Chang,* Robert H. Spencer,* Allen T. Lee, Margaret T. Barclay, Douglas C. Rees†

Mechanosensitive ion channels play a critical role in transducing physical stresses at the cell membrane into an electrochemical response. The MscL family of large-conductance mechanosensitive channels is widely distributed among prokaryotes and may participate in the regulation of osmotic pressure changes within the cell. In an effort to better understand the structural basis for the function of these channels, the structure of the MscL homolog from *Mycobacterium tuberculosis* was determined by x-ray crystallography to 3.5 angstroms resolution. This channel is organized as a homopentamer, with each subunit containing two transmembrane α helices and a third cytoplasmic α helix. From the extracellular side, a water-filled opening approximately 18 angstroms in diameter leads into a pore lined with hydrophilic residues which narrows at the cytoplasmic side to an occluded hydrophobic apex that may act as the channel gate. This structure may serve as a model for other mechanosensitive channels, as well as the broader class of pentameric ligand-gated ion channels exemplified by the nicotinic acetylcholine receptor.

The sensing of physical forces within a cell's environment is primarily mediated by a specialized class of membrane proteins known as mechanosensitive (MS) ion channels. MS channels have evolved the ability to transduce mechanical strain into an electrochemical response (*1*) enabling cells to respond to stimuli such as sound, touch, gravity, and pressure. Although several putative MS channels have been cloned, the large-conductance mechanosensitive channels (MscL) of prokaryotes have been most extensively characterized, primarily through the efforts of Kung and co-workers (*2–4*). MscL, first isolated

Howard Hughes Medical Institute and Division of Chemistry and Chemical Engineering, 147-75CH, California Institute of Technology, Pasadena, CA 91125, USA.

*These authors contributed equally to this work.
†To whom correspondence should be addressed. E-mail: dcrees@caltech.edu

from *Escherichia coli*, forms a nonselective ion channel of 2.5 nS conductance that is activated in vitro by the application of membrane tension. Localized within the inner membrane (*5, 6*), MscL is implicated in the regulation of osmotic pressure within the cell (*7*). MscL consists of a relatively small subunit (molecular mass of ~15 kD; Fig. 1) arranged as a homomultimer, possibly a hexamer, based upon cross-linking and electron microscopy studies (*5, 6, 8*). Hydropathy analysis indicates that MscL contains two transmembrane helices, and alkaline phosphatase fusion constructs suggest that both the NH_2- and COOH-termini are colocalized within the cytoplasm (*5*). Following the identification of MscL in *E. coli*, homologs have been found in more than 20 divergent prokaryotic species (*3, 9*). Their primary sequences exhibit a strong degree of conservation, especially within the putative transmembrane regions (Fig. 1). Additionally, the mechanosensitive properties for many of these homologs have been confirmed by patch-clamp studies, although differences in gating kinetics and pressure sensitivity are evident (*3*).

Structural characterization of MscL would establish not only the architecture of these channels but also aid in understanding the basic mechanism of mechanosensation. As recently demonstrated by the structure of the K^+ channel from *Streptomyces lividans* (KcsA) (*10*), bacterial channels have important advantages for structural analyses, including relatively simple architecture and expressibility. We identified a MscL homolog in the pathogenic bacterium *M. tuberculosis* (Tb-MscL) that contains 151 amino acids and exhibits an overall 37% sequence identity to the *E. coli* MscL (Eco-MscL). The crystal structure of Tb-MscL determined at 3.5 Å resolution establishes the structural organization of this integral membrane protein and suggests possible gating mechanisms for opening and closing the channel in response to membrane stress.

Structure determination. Protein crystals are stabilized by interactions involving specific amino acids on the protein surface, so that variations in these surface residues can profoundly influence the formation of lattice contacts during crystallization. We therefore adopted the strategy of surveying crystallization space by cloning (*11*), expressing, and purifying (*12*) MscL homologs derived from nine prokaryotic species, with the expectation that one or more of these natural variants would be more optimal for crystal formation. Each of the full-length MscL ion channel constructs was cloned and recombinantly expressed in a *mscL* knockout strain of *E. coli* (*2*). Those channels and conditions that were found more suitable for protein purification and crystallization were pursued further. After screening and refining approximately 24,000 crystallization conditions for the nine MscL homologs, using ~20 detergents, we obtained several different crystal forms of MscL. The *M. tuberculosis* homolog yielded crystals of the best diffraction quality, and these were used for the x-ray structure determination (*13*).

Native crystals of Tb-MscL grew in space group $I4_122$ (a = b = 212.96 Å, c = 96.43 Å) and diffracted to a resolution of ~7 Å using synchrotron radiation. Upon soaking these crystals in suitable heavy-atom compounds (Table 1), the space group unambiguously

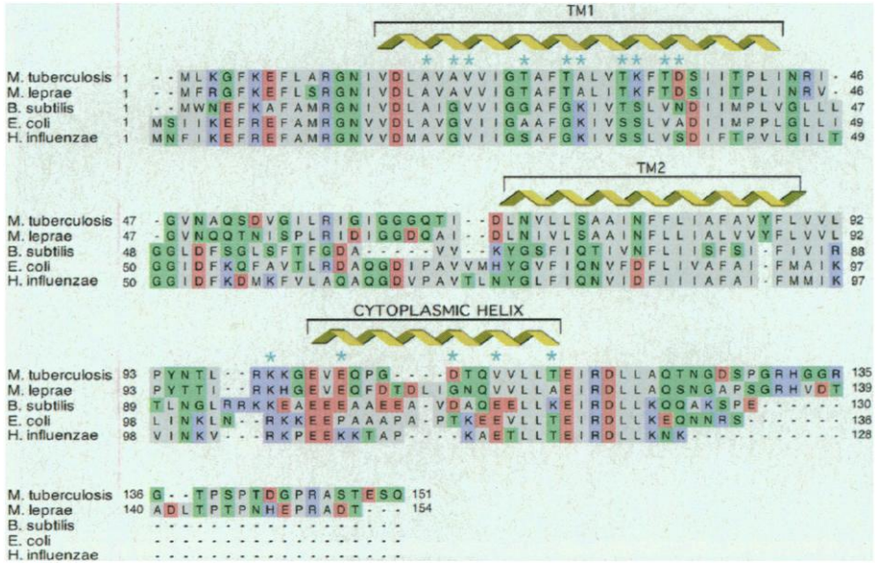

Fig. 1. The amino acid sequence (*40*) alignment for several MscL homologs produced using the program CLUSTALX (*41*). Residues are colored according to their acidic (red), basic (blue), polar (green), or hydrophobic (gray) character. The transmembrane and cytoplasmic helices for the Tb-MscL structure are indicated above the sequence alignment for reference, and pore-lining residues are denoted by an asterisk, including residues facing into the cytoplasmic helical bundle. The sequence for *M. leprae* was identified in a BLAST search of data from the Sanger Genome Project and is included for comparison with the *M. tuberculosis* sequence (identity = 73%). The following GenBank accession numbers reference the sequences used for the alignments: *B. subtilis*, Z83337; *E. coli*, P23867; *H. influenzae*, U32745; *M. tuberculosis*, AL021999.

	Diffraction data			
	$Na_3Au(S_2O_3)_2$	$(NH_4)_2WS_4$	$(CH_3)_3Pb$ acetate	Xe
Bragg spacing limits (Å)	20.0–3.5	20.0–3.5	20.0–7.0	20.0–7.0
Total observations	66,083	27,379	6,513	9,522
Unique observations	24,876	11,492	2,901	4,549
R_{sym} (%)	8.9	7.8	4.9	5.0
Completeness (%)	90	90	86	87

Generation of experimental electron density	
Phasing power	
$Na_3Au(S_2O_3)_2$	2.0
$(NH_4)_2WS_4$	2.3
Density correlation coefficient	45%
Overall figure of merit	0.56
Refinement statistics	
Single model	
R factor (20–3.5 Å)	40%
R_{free} (20–3.5 Å) (10%)	42%
Nine models	
R factor (20–3.5 Å)	26%
R_{free} (20–3.5 Å) (10%)	35%
Average *B* factor	68 Å^2
Model geometry	
Bond length deviation	0.009 Å
Bond angle deviation	1.6°

Table 1. Data collection and crystallographic analysis. All diffraction data used in the structural analysis were collected from single crystals at beamline 9-1 (λ = 0.98 Å) at the Stanford Synchrotron Radiation Laboratory (SSRL) except for the Xe data set, which was collected at beamline 7-1 (λ = 1.08 Å). Additional data sets were collected at beamline 5.0.2 at the Advanced Light Source (ALS) and also on laboratory x-ray sources (RAXIS II and RAXIS IV). All data sets were collected at −165°C and processed using the programs MOSFLM and SCALA (*39*). Because of their extremely fragile nature, the Tb-MscL crystals were stabilized with glutaraldehyde by vapor diffusing the crystals for at least 48 hours before heavy-atom soaking and data collection. In addition, the triethylene glycol concentration in the drop was gently increased to 38% by vapor diffusion for optimal cryo-protection for flash-cooling in liquid nitrogen or ethane. The incorporation and concentration of DDM in heavy-atom soaks was critical for maintaining the integrity and diffraction quality of the crystals.

changed to $I4_1$ with similar unit cell dimensions (a = b = 212.42 Å, c = 98.05 Å). We believe that the unsoaked Tb-MscL crystals contained a distribution of disordered molecules and that the binding of these heavy atoms stabilized a unique orientation, resulting in the lower symmetry space group. In an effort to strengthen protein lattice contacts and improve the overall order within these crystals, an extensive series of detergents, small organic molecules, and heavy-metal compounds were screened as additives. One of these compounds, $Na_3Au(S_2O_3)_2$, significantly improved the x-ray diffraction quality of the Tb-MscL crystals, to a limiting resolution of 3.5 Å. This compound was later found to bind at a set of crystal lattice contacts (Fig. 2A). In view of the superior diffraction quality, data collected from this soaked crystal was used as the "native" data set for the structure determination. With diffraction data collected from several different heavy-metal soaked crystals, phases were determined by the methods of multiple isomorphous replacement and anomalous scattering using the package PHASES (*14, 15*). Initial electron density maps clearly revealed that the asymmetric unit contained a single pentamer, corresponding to a solvent content of ~85%. Iterative fivefold noncrystallographic averaging, solvent flattening, and phase extension yielded electron density maps of excellent quality for model building (Fig. 2B). A chemical model was built using the program CHAIN (*16*), and the protein sequence registration was established by the presence of appropriate density in the electron density maps for the aromatic groups in the transmembrane helices.

The Tb-MscL structure refinement was complicated by a rapid decrease in intensity of the diffraction pattern with resolution, corresponding to an overall temperature factor of ~100 Å^2. Similar overall temperature factors were reported for the KcsA channel structure (*10*). The experimentally phased electron density maps, however, appeared to be of much better quality than would be expected for this temperature factor. This suggested that there was one predominant orientation for the channel in the crystal, likely stabilized by heavy-atom binding, with additional orientations that introduced a degree of positional disorder in the crystal. As a consequence, while the diffraction pattern remained rela-

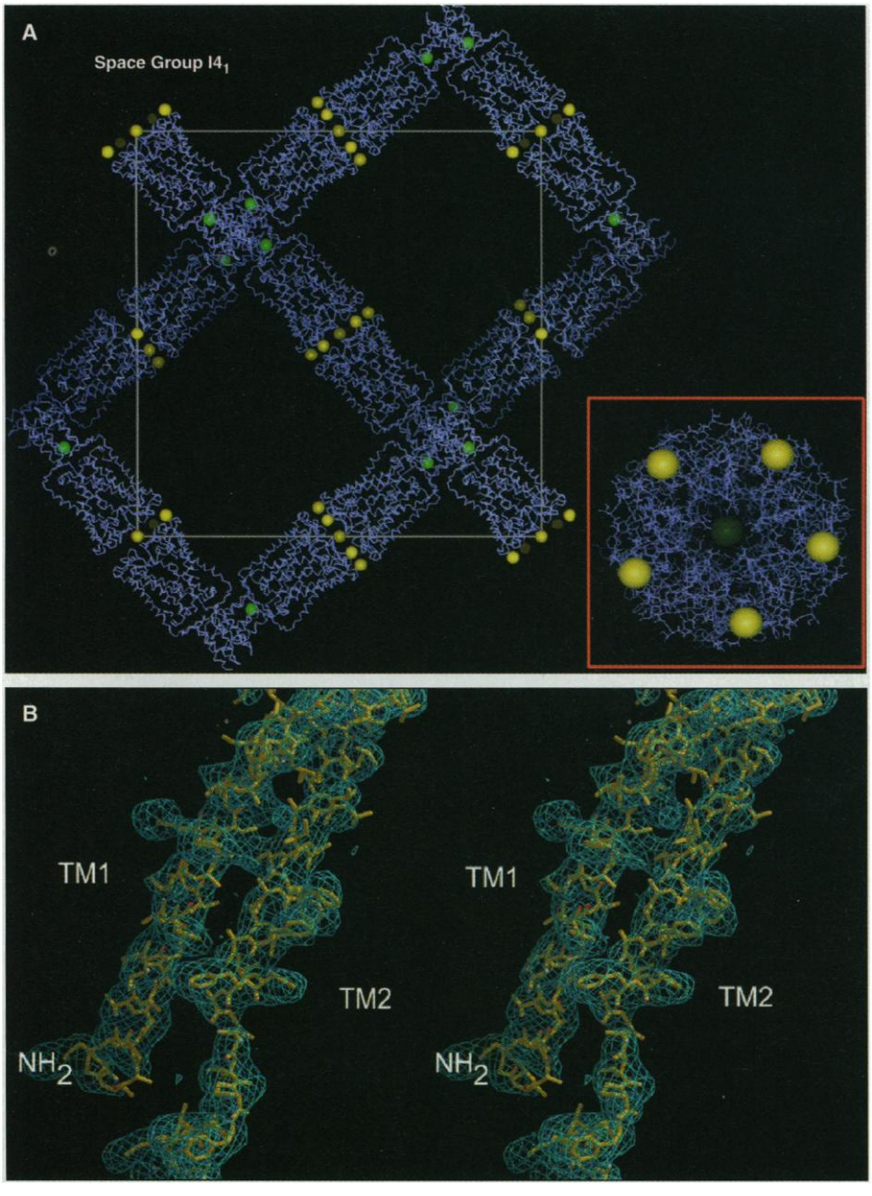

Fig. 2. Structure determination of Tb-MscL. (**A**) Packing diagram of Tb-MscL channels in the crystal. The space group is $I4_1$ and the unit cell is superimposed onto the crystal lattice. The yellow and green spheres indicate the positions of the bound $Na_3Au(S_2O_3)_2$ and $(NH_4)_2WS_4$ compounds, respectively. The binding of $Na_3Au(S_2O_3)_2$ to the crystal packing sites significantly improved the diffraction resolution from ~7.0 to 3.5 Å. The $(NH_4)_2WS_4$ bound within the cytoplasmic five-helix bundle of the channel. The inset represents the view from the extracellular side of the channel showing the relative positioning of the heavy atoms. (**B**) Stereoview of experimental electron density for the TM1 and TM2 transmembrane helices. The NH_2-terminal end of the model (residue 10) is labeled. The density is contoured at 1σ and rendered with BOBSCRIPT and RASTER-3D (*42–44*).

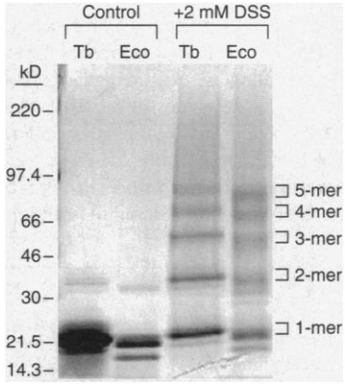

Fig. 3. Cross-linking analysis of the oligomeric state of purified MscL protein. Aliquots of Tb-MscL (10 μg) or Eco-MscL (3 μg) purified in 0.1% DDM were subjected to cross-linking with the homobifunctional, water-insoluble reagent DSS (2 mM final concentration). Reactions were performed in phosphate-buffered saline (pH 7.5) for 5 min at 4°C and subsequently quenched with 100 mM Tris (pH 7.5). The protein samples were resolved using a 4 to 15% polyacrylamide gel and visualized using Coomassie brilliant blue. For unknown reasons, monomers of the purified MscL proteins migrate as double bands on the gel, as reported previously (*2, 33*).

tively strong at lower resolution, the scattering contributions from this ensemble of protein and associated detergent interfered at higher resolution, resulting in a rapid decrease in intensities. Standard refinement algorithms are relatively poor at modeling positional disorder of this type (*17*) and, as a result, we were unable to refine any single model of Tb-MscL to values of R and R_{free} below ~40 and ~42%, respectively. In an effort to model multiple orientations, we simultaneously refined nine copies of the structure against the native data (*18–20*) with very strict fivefold noncrystallographic harmonic constraints applied between monomers within a channel, using the program X-PLOR (*21, 22*). After molecular dynamics refinement, an ensemble of similar models (average rms deviation between C_α atoms between models: <1.2 Å) was achieved with a crystallographic R factor of 26% and an R_{free} of 35% against the native Tb-MscL data. Residue positions in the α helical regions were well-defined in these models, whereas the loop regions were less well ordered. An averaged model with good stereochemistry was computed and used for structural analysis.

Structural organization of Tb-MscL. The pentameric arrangement observed crystallographically contrasts with earlier studies on Eco-MscL that had suggested a hexameric structure based on cross-linking experiments (*5*) and electron microscopy (*8*), although other studies were inconclusive on this point (*6*). Using the cross-linker disuccinimidyl suberate (DSS), we observed that cross-linked Tb-MscL and Eco-MscL proteins could each be separated by gel electrophoresis into a ladder of five bands, suggesting a pentameric association (Fig. 3). These results indicate that the organization of Tb-MscL observed in the crystal accurately represents the oligomeric state of the detergent-extracted protein.

The crystal structure establishes that Tb-MscL exists as a homopentamer composed of two domains, designated transmembrane and cytoplasmic. Both domains share the same fivefold axis relating subunits within the channel. Tb-MscL is ~85 Å in length, with the transmembrane and cytoplasmic domains accounting for 50 and 35 Å, respectively (Fig. 4). The diameters of the transmembrane and cytoplasmic domains are ~50 and 18 Å, respectively. The actual membrane-spanning region of Tb-MscL is ~35 Å in length and is primarily composed of hydrophobic residues in the transmembrane helices. As noted in other integral membrane proteins, there is a trend for aromatic residues to be localized near the membrane–aqueous phase interface (*23, 24*). In the case of Tb-MscL, aromatic residues predominate on the cytoplasmic side of the membrane, including two residues in TM1 (Phe^{27} and Phe^{34}) and five in TM2 (Phe^{79}, Phe^{80}, Phe^{84}, Tyr^{87}, and Phe^{88}).

Each subunit of Tb-MscL exhibits a relatively simple folding topology (Fig. 4). Starting from the NH_2-terminus at the cytoplasmic side, the first transmembrane helix (TM1, residues 15 through 43) crosses the membrane and creates the bulk of the pore. TM1 is connected to the second transmembrane helix (TM2, residues 69 through 89) by a loop (residues 44 through 68) that dips into the pore region. TM2 returns to the cytoplasm along the outside of the channel, and is followed by a second loop (residues 90 through 101) that connects to the cytoplasmic helix (residues 102 through 115). In view of the net

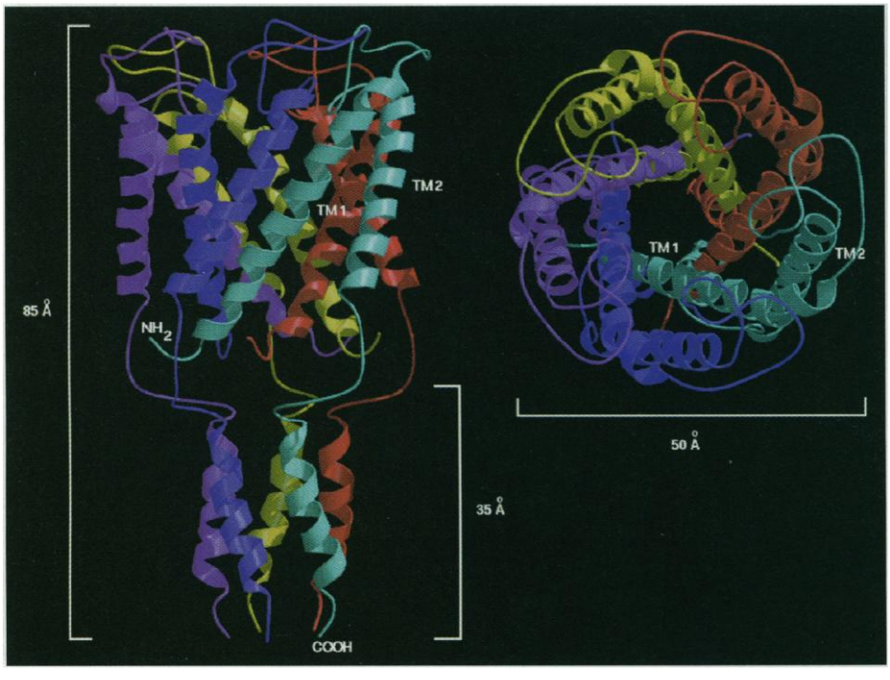

Fig. 4. Structure of the homopentameric mechanosensitive channel from *M. tuberculosis*. Side (left) and top (extracellular; right) views of Tb-MscL were rendered using BOBSCRIPT and RASTER-3D (*42–44*). The monomers within the channel are individually colored. The NH_2- and COOH-terminal ends of the cyan monomer are indicated, and the dimensions of the channel are shown.

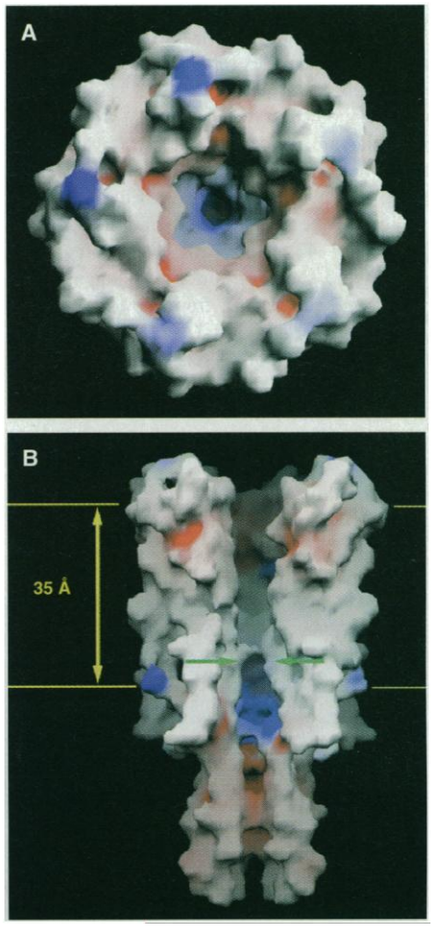

Fig. 5. (**A**) Molecular surface rendering of Tb-MscL viewed from the extracellular side of the membrane. The electrostatic potential was calculated using the program GRASP (*45*) assuming an ionic strength equivalent of 100 mM NaCl and a dielectric constant of 2 and 80 for protein and solvent, respectively. The surface coloring varies continuously from blue in more basic regions to red in more acidic areas. Note that the pore surface is highly polar and occluded at the cytoplasmic side of the channel. The deviation of the shading of the electrostatic potential surface from fivefold symmetry is a consequence of the off-axis placement of the light source used in this figure. (**B**) Cut-away side view of Tb-MscL to reveal the solvent-accessible surface within the channel. All atoms within a 50° wedge from the fivefold axis of the structure were removed for this representation. The yellow bars delineate the region of the hydrophobic surface where the lipid bilayer is presumed to be. The occluded region of the channel is indicated by the green arrows.

negative charge in this region (Fig. 5), it is possible that the cytoplasmic helix is stabilized in this structure by the low pH of the crystallization conditions. The remaining residues at the NH_2- and COOH-termini are presumably disordered. The sequence positions of the two transmembrane helices roughly agree with the predictions of the hydropathy analysis (*2, 5*). Additionally, the polypeptide fold through the transmembrane domain is threaded in the opposite direction to that observed in the KcsA channel (*10*).

The helical axes for TM1 and TM2 within each subunit are tilted by ~28° with respect to the molecular fivefold axis, whereas the cytoplasmic helices are tilted by ~15°. Each TM1 helix contacts four surrounding helices (Fig. 4). These contacts involve the TM1 helices of the two adjacent subunits (crossing angle = −43°) and two TM2 helices: one within the same subunit (crossing angle = 135°) and the second from an adjacent subunit (crossing angle = 169°) (*25*). The TM2 helices of neighboring subunits do not directly contact each other, but rather are separated by ~20 Å. The most extensive set of interactions in the transmembrane domain occurs between the TM1 and TM2 helices of adjacent subunits, with a buried surface area of 2300 Å^2. In contrast, the interactions between TM1 and TM2 helices within a subunit are less extensive and bury only 800 Å^2 between residues 34 through 36 and 77 through 79. The cytoplasmic domain consists of helices packed together at a crossing angle of ~24° to form a helical bundle that buries ~1700 Å^2 between adjacent monomers.

Pore structure. The pore of Tb-MscL appears to be extended along the fivefold axis through both the membrane and cytoplasmic domains. The radius of the transmembrane pore varies between ~2 to 18 Å and is partially occluded at the cytoplasmic surface (Fig. 5). In the transmembrane domain, the pore is lined with a series of hydrophilic residues from TM1, which include a series of four threonines (Thr^{25}, Thr^{28}, Thr^{32}, and Thr^{35}), a lysine (Lys^{33}), and an aspartate (Asp^{36}). Consequently, the interior surface of the channel has a distinctly polar character. Intriguingly, the abundance of threonine residues on this surface is reminiscent of the pore-forming M2 helix in the nicotinic acetylcholine receptor (*26, 27*). The hydrophobic residues Ile^{14} and Val^{21} create a constriction near the cytoplasmic surface at the NH_2-terminal end of TM1. In view of the small diameter (~2 Å) of the channel in this region, it appears likely that the structure of the channel represents a closed, or nearly closed, state.

The loop region between the TM1 and TM2 helices creates a flap that forms the extracellular surface of the pore. Residues 58 through 64 are found deep in the pore of the channel and are less ordered, perhaps reflecting the flexibility of three glycine residues (Gly^{62}, Gly^{63}, and Gly^{64}) at the bottom of the loop near Lys^{33} of TM1. Another interesting feature of the pore loop are two isoleucine residues (Ile^{59} and Ile^{61}) which face two other isoleucine residues (Ile^{38} and Ile^{39}) from the TM1 helix and may play some role in controlling the pore diameter.

Directly below the occluded region of the pore, there is a cluster of charged residues, including Arg^{98}, Lys^{99}, Lys^{100}, Glu^{102}, and Glu^{104}. The binding of oxyanionic heavy atoms from several different derivatives within this region of the cytoplasmic domain suggests a possible ligand-binding site, and the accessibility of this region could further imply that this part of the structure could potentially participate in part of the ion conduction pathway. In particular, a Xe-pressurized crystal (*28*) shows a tube of difference electron density along the fivefold axis of the cytoplasmic bundle (*29*). The juxtaposition of the transmembrane and cytoplasmic domains with coincident molecular axes, including the possible extension of the transmembrane channel through the cytoplasmic domain, resembles the proposed model for the interaction of the cytoplasmic NH_2-terminal domain and channel regions of the *Shaker* K^+ channel (*30*).

Relationship of structure to function. Unlike the cloned ligand- and voltage-gated ion channels that have been extensively characterized by a combination of electrophysiological and molecular biological techniques, the first mechanosensitive ion channel (Eco-MscL) was cloned relatively recently (*2*), and thus more limited information is currently available to relate MscL function to the structural model. However, mutagenesis studies with Eco-MscL have resulted in the mapping of several regions involved in the gating and pressure sensitivity of MscL (*31–33*). Considering the sequence similarity of Tb-MscL to Eco-MscL, these data yield significant insights into the domains responsible for MscL function.

The TM1 helix is one of the mostly highly conserved regions among MscL proteins, particularly at the NH_2-terminal end (*3*). Single-site mutagenesis of Eco-MscL along this region showed that mutations along one face of this helix significantly alter channel gating (*31, 32*). Based upon the Tb-MscL model, these mutations consistently map to residues facing the ion conduction pathway. Mutants that display a gain-of-function phenotype have the most profound effects at positions 22, 23, 26, and 30 of Eco-MscL (equivalent to positions 20, 21, 24, and 28 of Tb-MscL). It is believed that these mutants result in channels that readily open and thus inhibit growth due the loss of ions out of

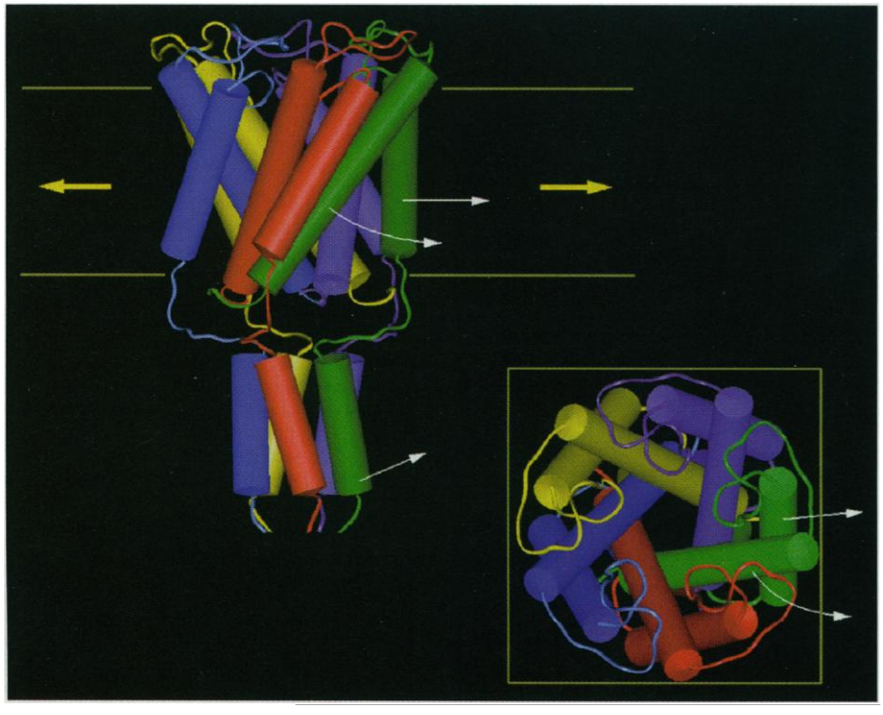

Fig. 6. Proposed model for the mechanosensitive gating of Tb-MscL. Side (left) and top (extracellular; right) views of the Tb-MscL channel with arrows indicating the proposed shift in relative helical position upon application of tension to the membrane. To provide accessibility to the ion conduction pathway, the position of the TM1 helices near the cytoplasm would need to shift radially from the molecular fivefold axis (normal to the membrane). Possible movement of the TM2 and cytoplasmic helices are also indicated. This figure was prepared using InsightII molecular modeling system (MSI, San Diego, CA).

the cell (*31*).

Because studies of the purified Eco-MscL channel reconstituted into lipid bilayers demonstrated that gating is intrinsic to this protein (*2, 34*), some integral structural rearrangement must occur to coordinate channel opening. Based upon the Tb-MscL structure, it would appear that the junction of the TM1 helices near the base of the channel can form a physical hydrophobic barrier or "gate" that occludes the channel, thereby restricting the permeation of ions through the pore. More significantly, several of the most severe gain-of-function mutants map within this hydrophobic apex (*31*), which supports the hypothesis that this region acts as the channel gate. Presumably, upon applying lateral tension to the membrane, rearrangement of the transmembrane region occurs such that the TM1 helices are pulled away from each other (Fig. 6), perhaps inserting between TM2 helices at the outer edge of the channel. Adjacent TM2 helices are separated by ~20 Å and, hence, could accommodate a repositioned TM1 helix (diameter of ~10 Å) between them. As a result of this proposed movement of the TM1 helices, the constriction of the central pore would be relaxed, thus allowing ions to cross the membrane. It has been reported that the cross-sectional area in the membrane occupied by MscL increases by ~350 Å^2 between the closed and open states of the channel (*4, 35*). Although the structure of the open state of Tb-MscL has yet to be determined, a change of this magnitude could be achieved upon channel opening by a relatively modest increase in the effective diameter of the transmembrane domain from ~50 to ~51 Å.

Pentameric organizations have been previously described for the important class of ligand-gated ion channels that include the nicotinic acetylcholine (AChR), serotonin ($5HT_3$), $GABA_A$, and glycine receptors (*36*). Beyond their common pentameric organization, the pore architecture of Tb-MscL exhibits strong similarities to that observed for the AChR (*37, 38*). In particular, the orientation, helix packing, and tilt angle of the M2 helices that have been proposed as forming the AChR pore correspond to those observed for the pore helices in Tb-MscL. The pore helices for both families appear to be lined with polar residues such as threonine or serine, and hydrophobic residues are present at the constriction in the pore that may act as the channel gate. The gating mechanism proposed for AChR involves a reorientation of the M2 helices that repositions the occluding hydrophobic residue, thereby leading to an open channel configuration. Although the detailed gating mechanisms undoubtedly differ between MscL and AChR, it seems quite plausible that they are both based on rearrangements of the pore helices that ultimately regulate the channel dimensions.

The structure of Tb-MscL provides a framework for understanding the transduction of mechanical stress on the lipid bilayer into protein conformational changes that control ion flux through the cell membrane. As a member of a family of mechanosensitive channels that are prevalent in bacteria, the structure of Tb-MscL should serve as a model for these related MscL channels and may additionally help to address aspects of the functional mechanism of nonhomologous, two-transmembrane-helix MS channels found in eukaryotes. Structural similarities in the pore regions between Tb-MscL and the family of pentameric ligand-gated ion channels also suggest that this structure will be useful for modeling gating mechanisms in a broad class of gated channels. As originally demonstrated with the structure of the bacterial photosynthetic reaction center (*23*), and most recently with the KcsA channel structure (*10*) and our work here, bacterial membrane proteins provide attractive systems for structural and functional characterization of more complex homologs of integral membrane proteins found in eukaryotes.

References and Notes

1. H. Sackin, *Annu. Rev. Physiol.* **57**, 333 (1995).
2. S. I. Sukharev, P. Blount, B. Martinac, F. R. Blattner, C. Kung, *Nature* **368**, 265 (1994).
3. P. C. Moe, P. Blount, C. Kung, *Mol. Microbiol.* **28**, 583 (1998).
4. S. I. Sukharev, P. Blount, B. Martinac, C. Kung, *Annu. Rev. Physiol.* **59**, 633 (1997).
5. P. Blount *et al.*, *EMBO J.* **15**, 4798 (1996).
6. C. C. Hase, R. F. Minchin, A. Kloda, B. Martinac, *Biochem. Biophys. Res. Commun.* **232**, 777 (1997).
7. M. Schleyer, R. Schmid, E. P. Bakker, *Arch. Microbiol.* **160**, 424 (1993).
8. N. Saint *et al.*, *J. Biol. Chem.* **273**, 14667 (1998).
9. MscL homologs were identified during BLAST searches of unfinished sequences from various genome sequencing projects including the following species: *Actinobacillus actinomycetemcomitans*, *Bordetella pertussis*, *Chlorobium tepidum*, *Deinococcus radiodurans*, *Enterococcus faecalis*, *Mycobacterium leprae*, *Porphyromonas gingivalis*, *Pseudomonas aeruginosa*, *Streptococcus pyogenes*, *Vibrio cholerae*, and *Yersinia pestis* (R. H. Spencer and G. Chang, unpublished material).
10. D. A. Doyle *et al.*, *Science* **280**, 69 (1998).
11. We identified the Tb-MscL homolog based upon a National Center for Biotechnology Information BLAST search of the *M. tuberculosis* genome project and isolated the coding region from genomic DNA (kind gift from S. Gordon, Institut Pasteur, Paris, France) using polymerase chain reaction–based techniques. The respective *mscL* genes from *E. coli*, *Synechocystis* sp., *Haemophilus influenzae*, and *Bacillus subtilis* were also cloned from genomic DNA. Plasmid clones containing the *mscL* genes from *E. carotovora*, *P. fluorescens*, and *Staphylococcus aureus* were obtained as a gift from C. Kung and P. C. Moe, University of Wisconsin–Madison, Madison, WI, and *mscL* from *Clostridium perfringens* was obtained as a gift from A. Okabe, Kagawa Medical School, Kagawa, Japan.
12. All MscL homologs were cloned into the pET19b vector (Novagen, Madison, WI) which added 23 residues at the NH_2-terminus of MscL including a decahistidine repeat and a consensus enterokinase cleavage site. Additionally, protein was expressed in *E. coli* using a *mscL* knockout mutant (lysogenized with λDE3) and induced via the addition of 0.1% 1-β-D-thiogalactoside (Anatrace, Maumee, OH) and 1% lactose. MscL was solubilized from 1- to 2-kg batches of cells using 1.0% dodecyl-β-D-maltoside (DDM; Anatrace, Maumee, OH) and purified with 0.1% DDM using nickel-chelate (Qiagen, Chatsworth, CA), ion exchange, and gel filtration chromatography.
13. Crystals of Tb-MscL were grown at 4°C by the sitting-drop method using protein at approximately 10 to 15 mg/ml and a final detergent concentration of 0.05% DDM. Protein was mixed in a ratio of 4:3 or 3:2 with a reservoir solution containing 100 to 120 mM ammonium sulfate, 23 to 27% triethylene glycol (TEG), 100 mM glycine (pH 3.6 to 3.8), and 1 to 3 mM $GdCl_3$ or $SmCl_3$ with D_2O as the solvent [R. Lutter *et al.*, *J. Mol. Biol.* **229**, 787 (1993)]. Crystals appeared within 5 days and matured to full size (~0.6 mm × 0.6 mm × 0.4 mm) within 2 weeks. Gel electrophoresis and protein immunoblot analysis with antibodies to a histidine tag (Qiagen) indicated that the crystals contained the full-length protein fused to a polyhistidine tag at the NH_2-terminal end.
14. The package PHASES was used for all phase calculations with multiple isomorphous and anomalous scattering data. Although we found eight derivatives, the data sets collected using crystals soaked in 10 mM $Na_3Au(S_2O_3)_2$, 5 mM $(NH_4)_2WS_4$, and 10 mM $(CH_3)_3Pb$ acetate were the most useful for phasing. The isomorphous and anomalous difference Patterson maps yielded strong peaks for the $Na_3Au(S_2O_3)_2$ and $(NH_4)_2WS_4$ sites, and the correct hand for this space group was established from anomalous difference Fourier maps. The initial experimentally phased electron density maps revealed a pentameric structure with a real-space correlation coefficient of 45% between subunits. Fivefold noncrystallographic symmetry averaging, solvent flattening, and incremental phase extension from 4.5 to 3.5 Å resolution were accomplished using locally written software (G. Chang, unpublished) to yield maps of excellent quality for model building. The final inversion *R* factor of 28% reflects the relatively large solvent content, the intensity distribution of the data, and the presence of partially ordered detergent in the crystal.
15. W. Furey and S. Swaminathan, *Methods Enzymol.* **277**, 590 (1997).
16. J. S. Sacks, *J. Mol. Graphics* **6**, 224 (1988).
17. J. P. Abrahams and A. G. W. Leslie, *Acta Crystallogr. D* **52**, 30 (1996).
18. M. Pellegrini, N. Gronbech-Jensen, J. A. Kelly, G. M. Pfluegl, T. O. Yeates, *Proteins* **29**, 426 (1997).
19. P. Gros, W. F. van Gunsteren, W. G. J. Hol, *Science* **249**, 1149 (1990).
20. J. Kuriyan *et al.*, *Proteins* **10**, 340 (1991).
21. A. T. Brünger, J. Kuriyan, M. Karplus, *Science* **235**, 458 (1987).
22. Numerous rounds of vector refinement were performed using the program X-PLOR to best fit the model into the electron density. Using this preliminary model, anisotropic correction to the diffraction data was applied to the diffraction data using X-PLOR. Wilson plots indicated a sharp drop of the mean diffraction intensities as a function of resolution with an overall *B* factor for the data of ~100 Å^2 depending on the data set. For reasons stated in the text, nine models were simultaneously refined against the native $Na_3Au(S_2O_3)_2$ data with very strict fivefold noncrystallographic harmonic constraints (2000 kcal/mole) within a pentamer and weak harmonic constraints (1.0 kcal/mole) between pentameric channel models. After simulated annealing refinement, the ensemble of closely related models (average rms deviation between all C_α atoms between models was <1.2 Å) had a crystallographic *R* factor of 26% and an R_{free} of 35% against the native data. Residues 10 to 118 of each subunit are included in the final model.
23. J. Deisenhofer, O. Epp, K. Miki, R. Huber, H. Michel, *Nature* **318**, 618 (1985).
24. M. S. Weiss *et al.*, *Science* **254**, 1627 (1991).
25. E. G. Hutchinson and J. M. Thornton, *Protein Sci.* **5**, 212 (1996).
26. S. Numa, *Harvey Lect.* **83**, 121 (1989).
27. J. P. Changuex, J. L. Galzi, A. Devillers-Thiery, D. Bertrand, *Q. Rev. Biophys.* **25**, 395 (1992).
28. S. M. Soltis, M. H. B. Stowell, M. C. Weiner, G. N. Phillips, D. C. Rees, *J. Appl. Crystallogr.* **30**, 190 (1997).

29. G. Chang, R. Spencer, A. Lee, M. Barclay, D. Rees, data not shown.
30. A. Kreusch, P. J. Pfaffinger, C. F. Stevens, S. Choe, *Nature* **392**, 945 (1998).
31. X. R. Ou, P. Blount, R. J. Hoffman, C. Kung, *Proc. Natl. Acad. Sci. U.S.A.* **95**, 11471 (1998).
32. P. Blount, S. I. Sukharev, M. J. Schroeder, S. K. Nagle, C. Kung, *ibid.* **93**, 11652 (1996).
33. C. C. Hase, A. C. LeDain, B. Martinac, *J. Membr. Biol.* **157**, 17 (1997).
34. ———, *J. Biol. Chem.* **270**, 18329 (1995).
35. W. J. Sigurdson, S. I. Sukharev, C. Kung, F. Sachs, *Biophys. J.* **72**, WP104 (1997).
36. H. A. Lester, *Annu. Rev. Biophys. Biomol. Struct.* **21**, 267 (1992).
37. N. Unwin, *Nature* **373**, 37 (1995).
38. ———, *J. Mol. Biol.* **257**, 586 (1996).
39. S. Bailey, CCP4 Project, *Acta Crystallogr. D* **50**, 760 (1994).
40. Single-letter abbreviations for the amino acid residues are as follows: A, Ala; C, Cys; D, Asp; E, Glu; F, Phe; G, Gly; H, His; I, Ile; K, Lys; L, Leu; M, Met; N, Asn; P, Pro; Q, Gln; R, Arg; S, Ser; T, Thr; V, Val; W, Trp; and Y, Tyr.
41. J. D. Thompson, T. J. Gibson, F. Plewniak, F. Jeanmougin, D. G. Higgins, *Nucleic Acids Res.* **25**, 4876 (1997).
42. R. M. Esnouf, *J. Mol. Graphics* **15**, 132 (1997).
43. P. J. Kraulis, *J. Appl. Crystallogr.* **24**, 946 (1991).
44. E. A. Merritt and D. J. Bacon, *Methods Enzymol.* **277**, 505 (1997).
45. B. Honig and A. Nicholls, *Science* **268**, 1144 (1995).
46. We thank A. Chirino for advice and computer support, J. G. Spencer for technical assistance, S. Gordon of the Institut Pasteur (Paris, France) for his kind gift of genomic DNA from *M. tuberculosis*, C. Kung and P. C. Moe from the University of Wisconsin–Madison for several cloned *mscL* homologs and for the *E. coli* knockout mutant for *mscL*, A. Okabe of the Kagawa Medical School (Kagawa, Japan) for providing cloned DNA of *mscL* from *C. perfringens*, and D. Dougherty and H. Lester for helpful discussions. We also thank the staff at the Stanford Synchrotron Radiation Laboratory (SSRL) and the Advanced Light Source (ALS) for their help in data collection. The synchrotron rotation camera facilities are supported by the U.S. Department of Energy (ALS and SSRL) and NIH (SSRL). G.C. and R.H.S. were supported by NIH postdoctoral fellowship grant GM18486 and an Amgen postdoctoral fellowship, respectively, during the initial stages of this project. Supported by the Howard Hughes Medical Institute. Protein Data Bank identifier for Tb-MscL is 1MSL.

29 October 1998; accepted 16 November 1998

Regulation of Polar Auxin Transport by AtPIN1 in *Arabidopsis* Vascular Tissue

Leo Gälweiler, Changhui Guan, Andreas Müller, Ellen Wisman, Kurt Mendgen, Alexander Yephremov, Klaus Palme*

Polar auxin transport controls multiple developmental processes in plants, including the formation of vascular tissue. Mutations affecting the *PIN-FORMED (PIN1)* gene diminish polar auxin transport in *Arabidopsis thaliana* inflorescence axes. The *AtPIN1* gene was found to encode a 67-kilodalton protein with similarity to bacterial and eukaryotic carrier proteins, and the AtPIN1 protein was detected at the basal end of auxin transport–competent cells in vascular tissue. AtPIN1 may act as a transmembrane component of the auxin efflux carrier.

Charles Darwin had proposed the concept of translocated chemical messengers in higher plants, which finally resulted in the discovery of polar auxin transport in the 1930s (*1*). The transport of auxin from the plant tip downward provides directional information, influencing vascular tissue differentiation, apical development, organ regeneration, tropic growth, and cell elongation (*2*, *3*). Polar auxin transport can be monitored by following the movement of radiolabeled auxin through tissues. Auxin transport is specific for the major auxin indoleacetic acid and various synthetic auxins, it requires energy, and it occurs with a velocity of 7 to 15 mm/hour (*2*). This transport can be specifically inhibited by synthetic compounds, known as polar auxin transport inhibitors, and by naturally occurring flavonoids (*4*). The current concept, known as the "chemiosmotic hypothesis," proposes that (i) the driving force for polar auxin transport is provided by the transmembrane proton motive force, and that (ii) the cellular efflux of auxin anions is mediated by saturable, auxin-specific carriers in shoots presumably located at the basal end of transport-competent cells (*2*). Immunocytochemical work with monoclonal antibodies to pea stem cell fractions indicated that the auxin efflux carrier is located at the basal end of auxin transport–competent cells (*5*).

Gene tagging. The phenotype of the *pin-formed* mutant of *Arabidopsis* can be mimicked by chemical inhibition of polar auxin transport (*6*). Analysis of auxin transport in *pin-formed* mutants suggests that an essential component for auxin transport is affected (*6*, *7*). To isolate the affected *AtPIN1* gene locus, we used the autonomous transposable element *En-1* from maize to generate mutants in *Arabidopsis thaliana*. We identified three independent transposon-induced mutants, *Atpin1::En134*, *Atpin1::En111*, and *Atpin1::En349*, that exhibited auxin transport–deficient phenotypes (*8*). These plants developed naked, pin-shaped inflorescences

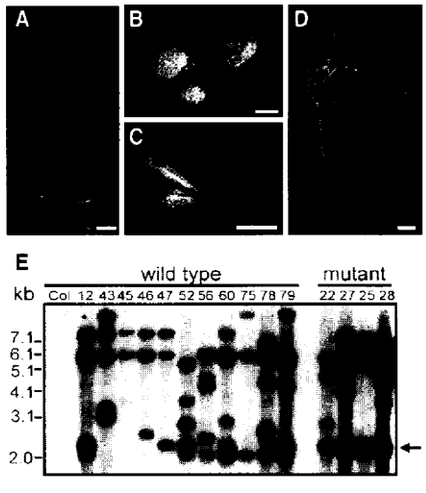

Fig. 1. Phenotypic and Southern blot analysis of the transposon insertional mutant *Atpin1::En134*. **(A)** The most obvious phenotypic aspect of the homozygous mutant represents the naked, pin-forming inflorescence with no or just a few defective flowers. **(B)** *Atpin1::En134* seedlings showed frequently aberrant cotyledon positioning or triple cotyledons. **(C)** A mutant cauline leaf exhibited abnormal vein branching resulting in the appearance of fused twin or triple leaves. Unusually, the leaf and "pin"-forming axillary shoot have formed in opposite positions. **(D)** Drastically fasciated inflorescence of an aged mutant. **(E)** Southern blot analysis of a segregating *Atpin1::En134* mutant population. The M_2 progeny of the heterozygous *Atpin1::En134* mutant showed 3:1 segregation for wild-type and mutant phenotype plants (*8*). The cetyltrimethylammonium bromide method (*23*) was used to isolate genomic DNA from plants showing the mutant (22, 27, 25 28) and wild-type (12, 43, 45, 46, 47, 52, 56, 60, 75, 78, 79) phenotype and from ecotype Columbia (Col) plants lacking *En-1* insertions. After Xba I digestion, the DNA was separated on a 0.8% agarose gel (2 μg per lane), transferred to a Nylon membrane and hybridized with a ^{32}P-labeled 3′-end probe of the *En-1* transposon (*24*). Only one fragment of 2.3 kb in length (marked by an arrow) was commonly detected in all 12 tested homozygous *Atpin1::En134* mutants and in 15 heterozygous plants (not all are shown), indicating cosegregation with the *Atpin1::En134* allele. Size bars represent 25 mm (A), 2.5 mm (B), and 10 mm [(C) and (D)].

L. Gälweiler, C. Guan, A. Müller, and K. Palme are at the Max-Delbrück-Laboratorium in der Max-Planck-Gesellschaft, Carl-von-Linné-Weg 10, D-50829 Köln, Germany. E. Wisman and A. Yephremov are at the Max-Planck-Institut für Züchtungsforschung, Abteilung Molekulare Pflanzengenetik, Carl-von-Linné-Weg 10, D-50829 Köln, Germany. K. Mendgen is at the Universität Konstanz, Fakultät für Biologie/Phytopathologie, D-78457 Konstanz, Germany.

*To whom correspondence should be addressed. E-mail: palme@mpiz-koeln.mpg.de